Applied Surface Science 597 (2022) 153630

Contents lists available at ScienceDirect

Applied Surface Science

journal homepage: www.elsevier.com/locate/apsusc

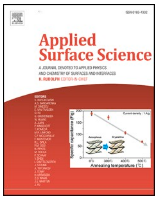

Full Length Article

Wet chemistry-based processing of tunable polychromatic carbon quantum dots for multicolor bioimaging and enhanced NIR-triggered photothermal bactericidal efficacy

Md Moniruzzaman [a,1], Sayan Deb Dutta [b,1], Ki-Taek Lim [b,*], Jongsung Kim [a,*]

[a] *Department of Chemical and Biological Engineering, Gachon University, 1342 Seongnam-daero, Seongnam-si, Gyeonggi-do 13120, Republic of Korea*
[b] *Department of Biosystems Engineering, Kangwon National University, Chuncheon-24341, Gangwon-do, Republic of Korea*

ARTICLE INFO

Keywords:
Wet-chemistry based processing
multicolor CQDs
Bioimaging
NIR-triggered photothermal
Bactericidal activity

ABSTRACT

A strategy for the processing of photoluminescence emission tunable multicolor carbon quantum dots has been adopted based on the controllable acidic strength [different ratio mixtures of sulfuric and phosphoric acids (S:P)] using a single polyphenolic precursor. 1,3,5-trihydroxybenzene, a three-fold symmetric (C_{3h} symmetry) triangulogen bearing –OH group at the meta position, was judiciously chosen to undergo dehydration facilitated condensation and carbonization suitably via a tri-molecular reaction route in a dehydrating acid medium. Polyaromatic-polyphenolic CQDs with multicolor emissions [blue (B-CQDs), green (G-CQDs), and yellow (Y-CQDs)] could be rapidly obtained through a facile wet chemistry-based thermal heating process. The mechanism of regulated bottom-up growth of CQD particles involved tri-molecular ring cyclization. These multicolor luminous CQD probes enabled intense multicolor cellular imaging throughout the entire visible range because of their good biocompatibility, photostability, and effective intracellular distribution. Moreover, Y-CQDs with larger polyaromatic sp^2 domains and higher oxidized surfaces exhibited a high photothermal conversion efficiency (PCE $\sim 32.6 \pm 1$ %) and thus exhibited remarkable NIR-light responsive photothermal bactericidal activity. Our results demonstrate that hyperthermia-induced bactericidal activity is due to the elevated reactive oxygen species (ROS) amplification and membrane damage of *Bacillus subtilis*. This study provides a potential alternative for the multicolor imaging guided CQDs-based phototheranostic.

1. Introduction

Multicolor emissive carbon nanostructures with tunable emission properties have received considerable attention owing to their diverse applications, including sensing [1], bioimaging [2], light emitting devices (LEDs) [3], and photocatalysis [4]. To date, significant efforts have been devoted to synthesizing multicolor carbon dots (CDs), and several strategies have been reported, such as proper precursor selection [5], surface passivation [6], chromatographic separation [7], solvatochromism [8], solvent engineering [9], reagent ratio optimization [10], chemical doping [11], pH control [11,12], temperature-control [13], reaction time monitoring [2], and concentration variation [14]. One of the common but complex methods is to adopt the separation of CDs based on different size distributions via sophisticated silica column chromatographic separation techniques. Yuan et al. separated multicolor triangular carbon quantum dots (CQDs) with different sizes, and proposed that the optical properties are related to the particle size (quantum confinement effect) and band edge exciton state [7]. However, this technique has some disadvantages, including prolonged reaction, difficult purification, and different reaction conditions for different emissions. In this regard, an alternative method can be adopted to screen suitable precursors. For instance, Jiang et al., synthesized multicolor (blue, green, and red) CDs by selecting suitable precursor, phenylenediamine isomers (o-, m-, and p-) and proposed that the tunable photoluminescence (PL) emission is related to particle size and N content [15]. As N is a heteroatom, N-doping has a very important role in tuning the PL emission by altering the band gap, interacting with solvents (solvatochromism), and inducing fast charge transfer over the surface electronic states. Thus, numerous N-containing precursors have been utilized to synthesize multicolor CDs, such as diaminonaphthalene

---

* Corresponding authors.
E-mail addresses: ktlim@kangwon.ac.kr (K.-T. Lim), jongkim@gachon.ac.kr (J. Kim).

[1] These authors contributed equally to this manuscript.

https://doi.org/10.1016/j.apsusc.2022.153630
Received 7 March 2022; Received in revised form 28 April 2022; Accepted 8 May 2022

isomers [3], trinitropyrene [9], urea [16], p-phenylenediamine [17], o-phenylenediamine [18], indole [19], polythiophene derivatives [20], and ethylene diamine tetraacetic acid [21]. In contrast, polyphenolic precursors have been used to a lesser extent for this purpose, and only a few reports exist in the literature. For instance, 1,3,5-trihydroxybenzene, a trihydroxyphenol, was used for the synthesis of full-color CQDs with narrow-bandwidth emission via solvothermal treatment followed by sophisticated purification using silica column chromatography [7]. Therefore, the exploration of diverse precursor scopes with controllable reaction conditions for the synthesis of multicolor CQDs are required.

Owing to their non-toxicity, photostability, and biocompatibility, luminescent CQDs have been extensively used in cell counting, multichannel sensing, cell sorting, clinical diagnostics, and other biomedical applications via multicolor bioimaging. For multicolor bioimaging, CQDs with excitation-dependent emission have been normally used; however, the PL emission intensity is often reduced in the longer wavelength range, which limits their application in multicolor bioimaging [22,23]. In this regard, Pan et al. produced excitation-dependent CQDs using formamide and citric acid via microwave techniques and applied them to multiple color cellular imaging [24]. Numerous efforts have been made to produce conjugated polymer dots or CQDs with multicolor PL emission; however, their synthesis process often involves a very complex technique [25]. Therefore, for multicolor PL emissive CQDs, a simplified, easy operable, equipment free, and unprolonged synthesis process is highly desirable.

Traditional antibiotics (naturally or chemically derived) or a mixture of antibiotics are less effective against drug-resistant bacterial strains as pathogenic bacteria have achieved resistance to conventional antibiotics by mutation or by obtaining resistance genes from other microorganisms. Recently, photo-responsive materials, particularly photothermal agents (PTAs), have been extensively used as rapid, minimally invasive, and effective therapeutic agents for the sterilization of antibiotic-resistant bacteria for the treatment of infectious diseases [26]. To date, numerous photothermal materials, such as noble-metal-based nanomaterials [27], metallic sulfides [28], polymeric nanocomposites [29], metallic oxides [30], phosphorus [31], and carbon-based nanomaterials [32], have been used to transform light energy into thermal energy under external light stimulation for combating pathogenic bacterial infections. Among these, carbon-based nanomaterials have received considerable attention owing to their superior physicochemical features, good biocompatibility, and comparatively higher biosafety [32]. In addition, the use of ultraviolet–visible (UV–Vis) illumination to eradicate pathogenic bacteria is not appropriate in vivo because of its harmful effects on biological tissues. Therefore, near infrared (NIR) light ($\lambda = 700–1100$ nm) is preferred in clinical practice because of its low absorption and scattering coefficients for biological tissues [33]. Although NIR-responsive PTAs, which include gold nanorods, carbon nanotubes, indocyanine green dyes, and metal nanostructures, have been explored for photothermal therapy, their clinical applications are limited because of their expensiveness and cytotoxicity [26]. Therefore, CQD materials with high photo-conversion efficiency in the NIR region, low toxicity, low cost, and easy synthesis form an important and necessary research topic [26].

Considering the above facts, we adopted a strategy for the preparation of multicolor CQDs [blue (B-CQDs), green (G-CQDs), and yellow (Y-CQDs)] with tunable PL-emission by regulating the acid strength of the precursor (1,3,5-trihydroxybenzene) solution using various ratio mixtures of sulfuric and phosphoric acids (S: P). Multicolor emissive CQDs have been utilized as promising luminous probes for multicolor cellular imaging because of their good biocompatibility, photostability, and effective intracellular distribution. Moreover, the as-prepared CQDs presented a high photothermal conversion efficiency of NIR light energy (808 nm) into thermal energy and thus exhibited remarkable photothermal bactericidal activity. Y-CQDs with larger polyaromatic sp^2 domains and higher oxidized surfaces exhibited a high photothermal conversion efficiency (PCE ~ 32.6 ± 1%) and thus exhibited remarkable NIR-light responsive photothermal bactericidal activity. Scheme 1 illustrates the fabrication process of the multicolor CQDs, which were designed for potential multicolor bioimaging and photothermal bactericidal activity.

2. Experimental

2.1. *Synthesis of multicolor CQDs*

In a typical synthesis method, the polyphenolic precursor (1,3,5-trihydroxybenzene, 200 mg) was dispersed in 2 mL of water in a 100-mL glass beaker and 2 mL of various ratio mixtures of conc. H_2SO_4 and H_3PO_4 acids (H_2SO_4:H_3PO_4 ratios were 0 mL: 2 mL, 0.4 mL: 1.6 mL, 0.8 mL: 1.2 mL, 1.0 mL: 1.0 mL, 1.2 mL: 0.8 mL, 1.6 mL: 0.4 mL, and 2.0 mL :0 mL) were added. Subsequently, the pale yellowish colored solution was placed in a hot air oven preheated at 190 °C, and the reaction time was monitored for 90 min. After the thermal reaction, the glass beaker was immediately taken out for natural cooling. Then, deionized (DI) water (5 mL) was added to each beaker, followed by high-speed centrifugation at 13000 rpm to obtain the black mass of the CQDs. Subsequently, the products were washed with DI water and dialyzed using a cellulose ester membrane (molecular weight cut-off of 100–500 Da) for 48 h. The dialyzed product was dried and dispersed in ethanol, followed by centrifugation at 3000 rpm for 5 min to remove unwanted large particles. Finally, the filtrate was dried to obtain a black powder of the CQDs, as shown in **Fig. S1 (Electronic Supplementary Information, ESI†).** CQDs were dispersed in 0.5% ethanolic aqueous solution for further experiments. The as-prepared CQDs showed different color emissions, such as blue (B-CQDs, H_2SO_4: H_3PO_4 ratios of 0 mL: 2 mL), green (G-CQDs, H_2SO_4: H_3PO_4 ratios of 1.0 mL: 1.0 mL), and yellow (Y-CQDs, H_2SO_4: H_3PO_4 ratios of 2 mL: 0 mL) in absolute ethanol.

3. Results and discussion

3.1. *Formation of multicolor CQDs*

The polyphenolic compound, 1,3,5-trihydroxybenzene (a triangulogen), with a suitable molecular three-fold symmetry (C_{3h}; symmetry elements: E, C_3, C_3^2, σ_h, S_3, S_3^{-1}), was judiciously chosen. During high-temperature thermal reactions, several 1,3,5-trihydroxybenzene molecules underwent six-membered ring cyclization via the elimination of active –H and –OH groups through a tri-molecular reaction route in a sulfuric acid and phosphoric acid mixture medium, as shown in Fig. 1 [7]. The PL emission was tuned by simply varying the acid strength of the reaction medium using various ratio mixtures of sulfuric and phosphoric acids, as shown in **Fig. S2 (ESI†).** The formation of CQDs was investigated using ^{1}H-nuclear magnetic resonance (NMR) and ^{13}C NMR spectroscopy, as shown in Fig. 2 **and Fig. S3 (ESI†).** The ^{1}H NMR spectra (Fig. 2**a)** of 1,3,5-trihydroxybenzene (precursor) exhibited two signals at $\delta = 5.7$ and 9.01 ppm due to two different proton environments. The ^{1}H NMR spectra **(**Fig. 2**b, c, and d)** of CQDs showed numerous new signals compared to the precursor due to different proton environments. Numerous proton signals at approximately $\delta = 7.2–8.0$ ppm represent polyaromatic proton, which indicates that several 1,3,5-trihydroxybenzene molecules were fused to form a large polyaromatic CQDs domain. These polyaromatic proton signals were less emerging in the case of B-CQDs, which suggests the formation of smaller polyaromatic CQD domains due to lower dehydrating capability of phosphoric acid. Moreover, precise investigation also revealed the gradual emergence of numerous peaks with an increase in the percentage of H_2SO_4 (higher dehydrating capability), which corresponds to the formation of larger CQD polyaromatic domains by the fusion of more 1,3,5-trihydroxybenzene molecules via dehydration-mediated growth. Numerous emerging signals were also observed at approximately $\delta = 6.2–7.0$ ppm, which were related to proton signals of hydroxyl and sulfonic acid/thiol

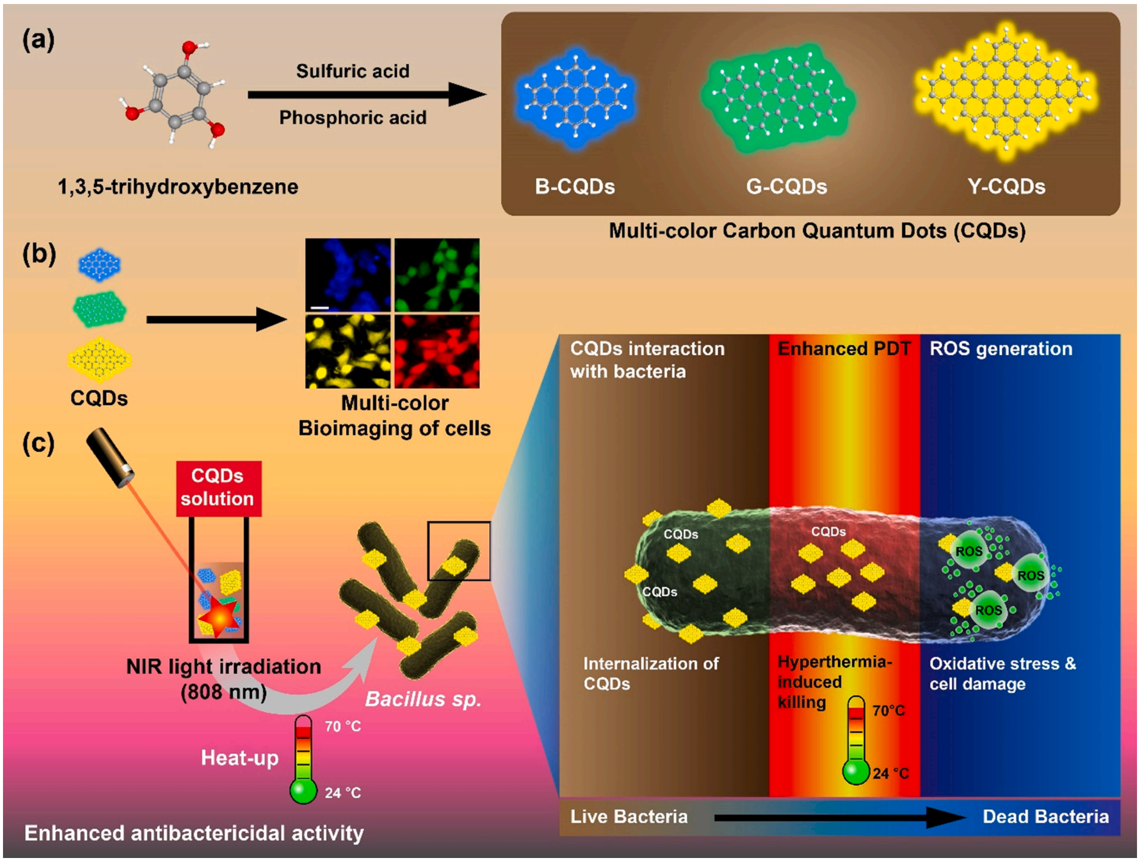

Scheme 1. Schematic elucidation for the fabrication of multicolor CQDs [Blue (B-CQDs), Green (G-CQDs), and Yellow (Y-CQDs)] with potential multicolor bio-imaging and photothermal bactericidal activity.

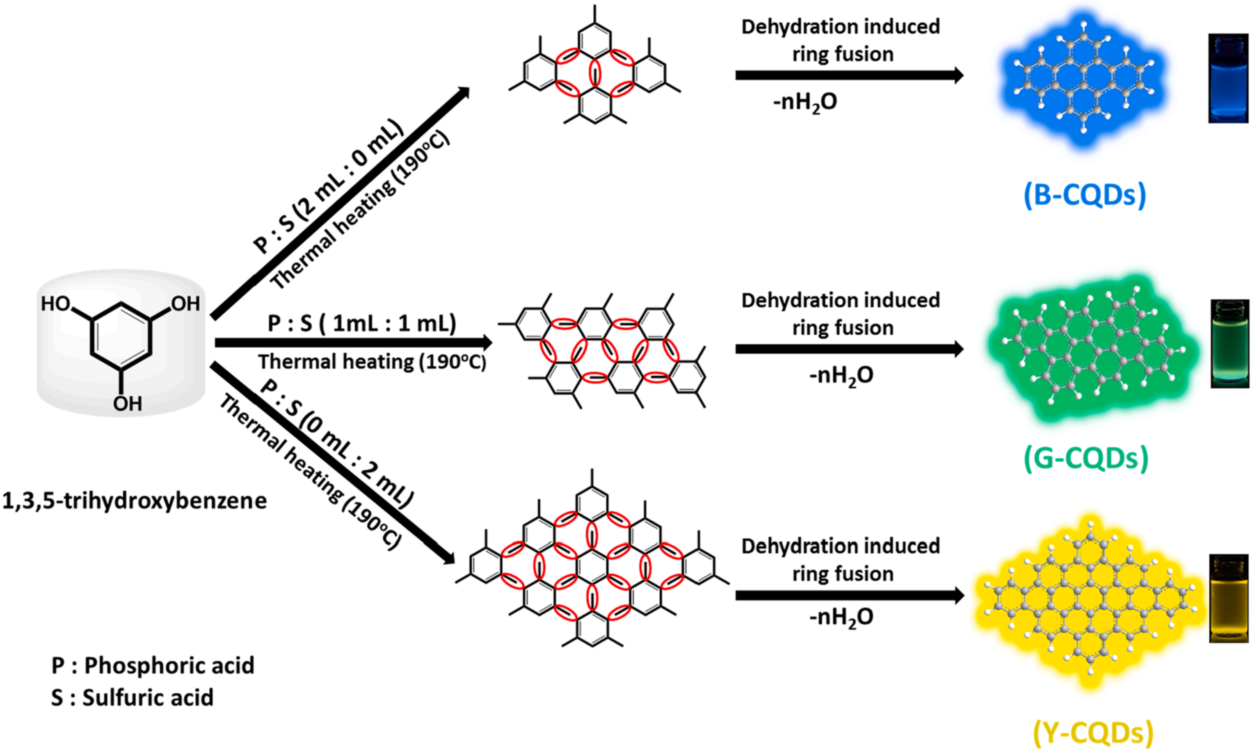

Fig. 1. Schematic illustration for the formation mechanism of multi-fluorescence CQDs via tri-molecular reaction route.

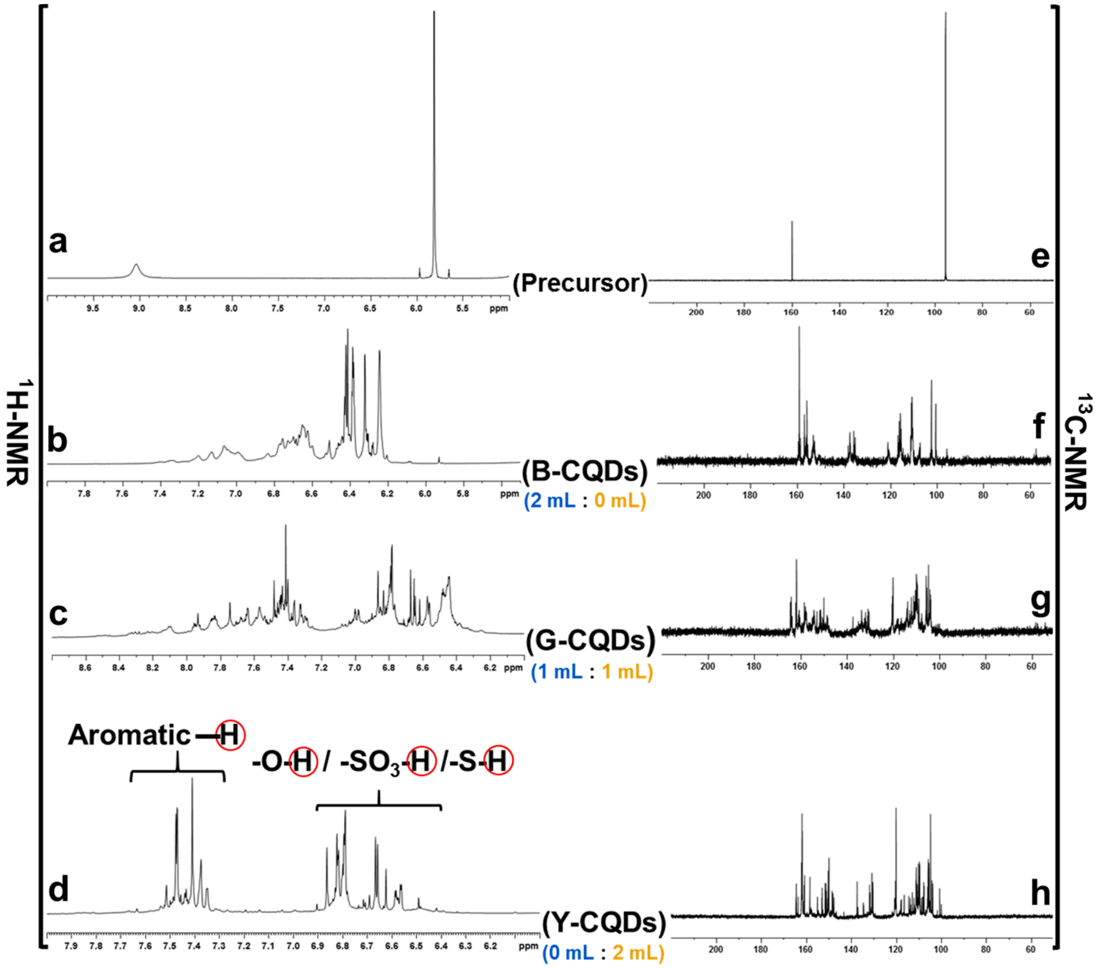

Fig. 2. ^{1}H NMR spectra of (a) 1,3,5-trihydroxybenzene (b) B-CQDs, (c) G-CQDs, (d) Y-CQDs. ^{13}C NMR spectra of (e) 1,3,5-trihydroxybenzene (f) B-CQDs, (g) G-CQDs, (h) Y-CQDs.

groups. By scrutinizing all the ^{1}H NMR spectra of CQDs prepared under various ratio mixtures of S: P acid medium, it can be concluded that there were three main types of ^{1}H NMR spectral structures corresponding to B-CQDs, G-CQDs, and Y-CQDs. Moreover, the ^{13}C NMR spectra (Fig. 2**e)** of 1,3,5-trihydroxybenzene molecule also showed two carbon peaks at $\delta = 94$ and 159 ppm due to two different carbon environments, whereas the CQDs (Fig. 2**f, g, and h)** exhibited numerous new signals due to different carbon environments. Numerous emerging resonance signals detected at approximately 145–166 ppm in the ^{13}C NMR spectra of CQDs represent the polyaromatic sp^2 hybridized carbon atoms connected to –OH groups at the edges, indicating that several 1,3,5-trihydroxybenzene molecules were fused to form a large polyaromatic CQD domain. The signals detected in this region gradually intensified from B-CQDs to Y-CQDs, indicating the gradual formation of larger dots. Moreover, in contrast to 1,3,5-trihydroxybenzene, multiple peaks were observed in the ^{13}C NMR spectra of CQDs in the region of 115–140 ppm, indicating the development of intact sp^2 polyaromatic domains. Similarly, the ^{1}H NMR and ^{13}C NMR spectra of CQDs prepared in various ratio mixtures (H_2SO_4: H_3PO_4 ratios, (i) 0.4 mL: 1.6 mL, (ii) 0.8 mL: 1.2 mL, (iii) 1.2 mL: 0.8 mL, and (iv) 1.6 mL: 0.4 mL) are shown in **Fig. S3 (ESI†)**. ^{1}H NMR and ^{13}C NMR spectra **(**Fig. 2 **and Fig. S3 (ESI†)** of CQDs prepared in various ratio mixtures, show that three distinct CQDs are produced, which contributes to the evolution of three distinct color emissions [blue (B-CQDs), green (G-CQDs), and yellow (Y-CQDs)].

3.2. *Structural characteristics of CQDs*

Comprehensive characterizations, such as high-resolution transmission electron microscopy (HR-TEM), X-ray diffraction (XRD), and Raman spectroscopy, were performed to investigate the morphology and structure of CQDs. HR-TEM image **(**Fig. 3**)** displayed unique crystalline trilateral and/or quadrilateral structure of B-, G-, and Y-CQDs with size distributions of 3–5, 4–7, and 6–10 nm, respectively. The HR-TEM images and the Fast Fourier Transform (FFT) pattern show well resolved lattice spacing of 0.21 nm for all three distinct CQDs (B-, G-, and Y-CQDs), demonstrating the inter-planar spacing of the (1 0 0) plane, which relates to the defect-free graphene structure [7,34]. The gradual growth of the CQDs from B-CQDs to Y-CQDs, as reflected in the HR-TEM images, was in good agreement with the quantum size effect-induced intrinsic emission behavior, clearly indicating the quantum confinement effect. The XRD pattern **(**Fig. 3**d)** of the precursor contained numerous highly crystalline peaks around θ = 16.9°, 21.7°, 23°, 25.1°, 27.2°, and 28.1°, which were converted into a broad peak after the thermal heating process in dehydrating acid, indicating the formation of polyaromatic carbon nanostructured quantum dots. The XRD spectra of B-, G-, and Y-CQDs exhibited broad peaks, suggesting that the (0 0 1) facet of the graphene structure was situated at approximately 27.2°, 23.3°, and 22.4°, respectively. The progressive narrowing of the XRD spectra from B-CQDs to Y-CQDs suggests a gradual increase in the crystalline nature and a larger conjugated domain of the particle [7]. The Raman spectra **(**Fig. 3**e)** of all the CQDs were analyzed to examine their inherent structure, which exhibited significant graphitization. The

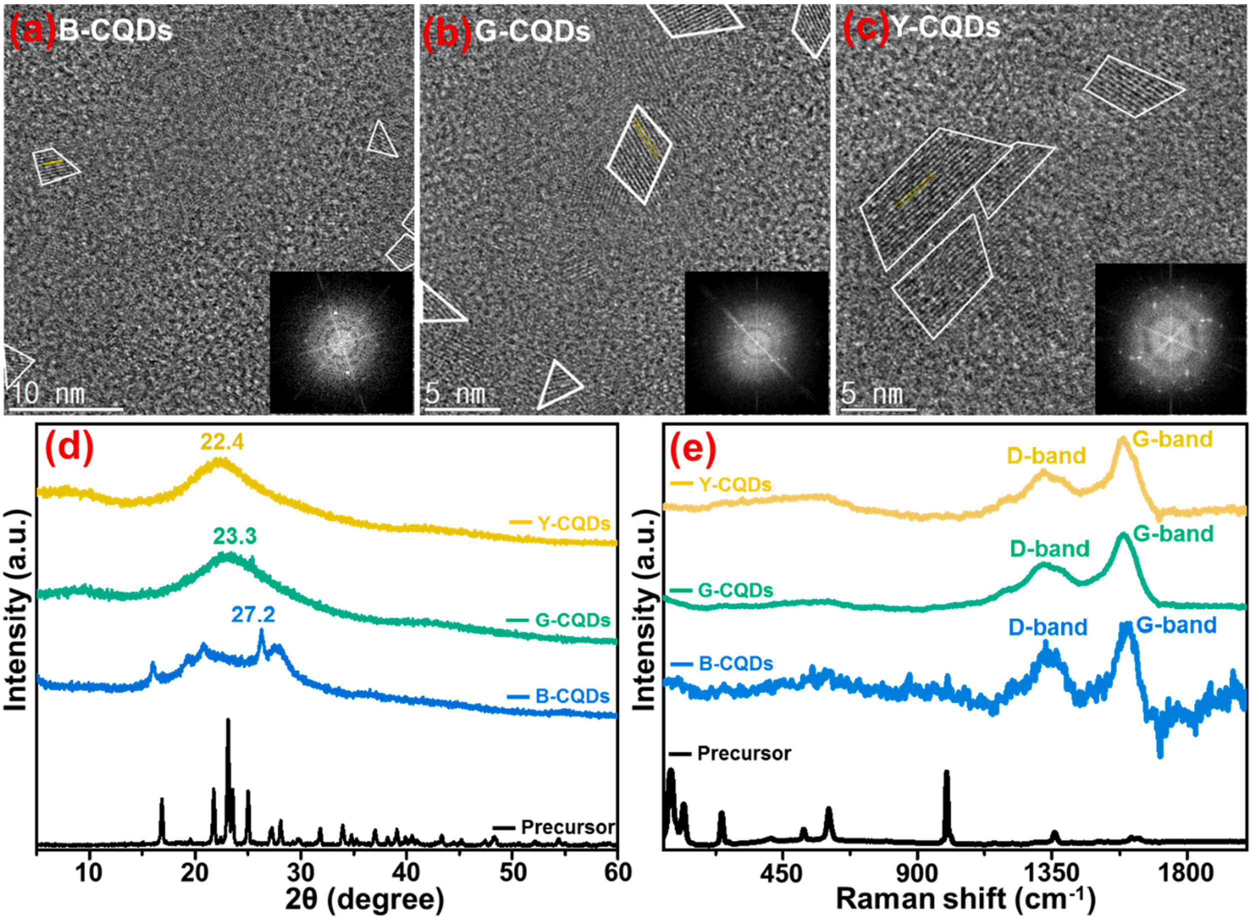

Fig. 3. HR-TEM images of (a) B-CQDs, (b) G-CQDs, and (c) Y-CQDs (white contour lines represent the morphology). Insets are the fast Fourier transform (FFT) images of the CQDs; (d) XRD pattern, (e) Raman spectra.

Raman spectra of all the CQDs displayed two common peaks located at 1330 and 1590 cm^{-1}, corresponding to the D-band and G-band, respectively. The D-band implies the existence of sp^3 carbon frameworks (disordered carbons) or defects due to surface oxidation and C–O stretching vibrations. The G-band represents the existence of sp^2 hybridized carbon networks, which indicates a significant degree of graphitization. The I_G/I_D ratio was higher than one for all three distinct CQDs, indicating the development of good-quality of graphene-structured CQDs, as evident from the HR-TEM images [7]. Similarly, XRD and Raman spectra of CQDs prepared in various ratio mixtures (H_2SO_4: H_3PO_4 ratios (i) 0.4 mL: 1.6 mL, (ii) 0.8 mL: 1.2 mL, (iii) 1.2 mL: 0.8 mL, and (iv) 1.6 mL: 0.4 mL) are shown in **Fig. S4 (ESI†).**

3.3. *Surface functional group analysis*

The surface functional groups and chemical composition of all the CQDs were inspected using Fourier-transform infrared (FT-IR) and X-ray photoelectron (XPS) spectra (Fig. 4). As shown in (Fig. 4**a**), the FT-IR spectra of the three CQDs exhibited similar peaks, suggesting that they consisted of some identical chemical bonds or functional moieties. The FT-IR spectra exhibited characteristic bands of O–H and C–O/C–C stretching vibrations at approximately 3403 and 1170 cm^{-1}, respectively. The peak around 1590 cm^{-1} was ascribed to the stretching vibration mode of C = C bonds belonging to polyaromatic carbon frameworks containing phenolic –OH groups at the zigzag edges [35]. The vibrational stretching of the $-SO_3H$ groups was also observed at approximately 1360 and 1026 cm^{-1} in the case of G- and Y-CQDs, respectively, which were missing in B-CQDs, implying that G- and Y-CQDs were primarily composed of –OH and $-SO_3H$ functional groups [36,37]. The FT-IR spectra of CQDs prepared in various ratio mixtures (H_2SO_4: H_3PO_4 ratios (i) 0.4 mL: 1.6 mL, (ii) 0.8 mL: 1.2 mL, (iii) 1.2 mL: 0.8 mL, and (iv) 1.6 mL: 0.4 mL) are shown in **Fig. S5a (ESI†).**

The elemental composition and valence states were investigated using XPS analysis. The XPS total survey spectra (Fig. 4**b**) of the G- and Y-CQDs were composed of S2p, C1s, and O1s peaks, indicating that the G- and Y-CQDs consisted of three elements (S, C, and O). The B-CQDs were mainly composed of C and O. The small peaks corresponding to P were due to the phosphoric acid treatment. The elemental valence states of C1s (Fig. 4**c**) of all the CQDs were investigated using high-resolution XPS spectra, which showed three bands at 284.9, 286.8, and 289 eV, implying the existence of C = C, C–C/C–S, and C–O, respectively [37]. The high-resolution S2p XPS spectra (Fig. 4**d**) of the G- and Y-CQDs showed two main bands at 164.4 and 169 eV, corresponding to –SH and $C-SO_3H$, respectively [38,39]. Thus, according to the FT-IR and XPS spectral investigations, it was concluded that B-CQDs were composed of –O–H, C = C, C–C, and C–O chemical bonds, whereas G- and Y-CQDs were composed of C = C, C–O, C–S, –SH, and $-C-SO_3H$. Similarly, The XPS total survey and high-resolution XPS spectra (C1s and S2p) of CQDs prepared in various ratio mixtures (H_2SO_4: H_3PO_4 ratios (i) 0.4 mL: 1.6 mL, (ii) 0.8 mL: 1.2 mL, (iii) 1.2 mL: 0.8 mL, and (iv) 1.6 mL: 0.4 mL) are shown in **Fig. S5b (ESI†), and Fig. S6 (ESI†)].**

3.4. *Optical properties*

UV–Vis absorption spectra were recorded to examine the optical properties of all the differently emissive CQDs. The UV–Vis absorption spectra (Fig. 5**a**) of B-CQDs, G-CQDs, and Y-CQDs dispersed in ethanol exhibited broad peaks at 266, 293, and 305 nm, respectively. The

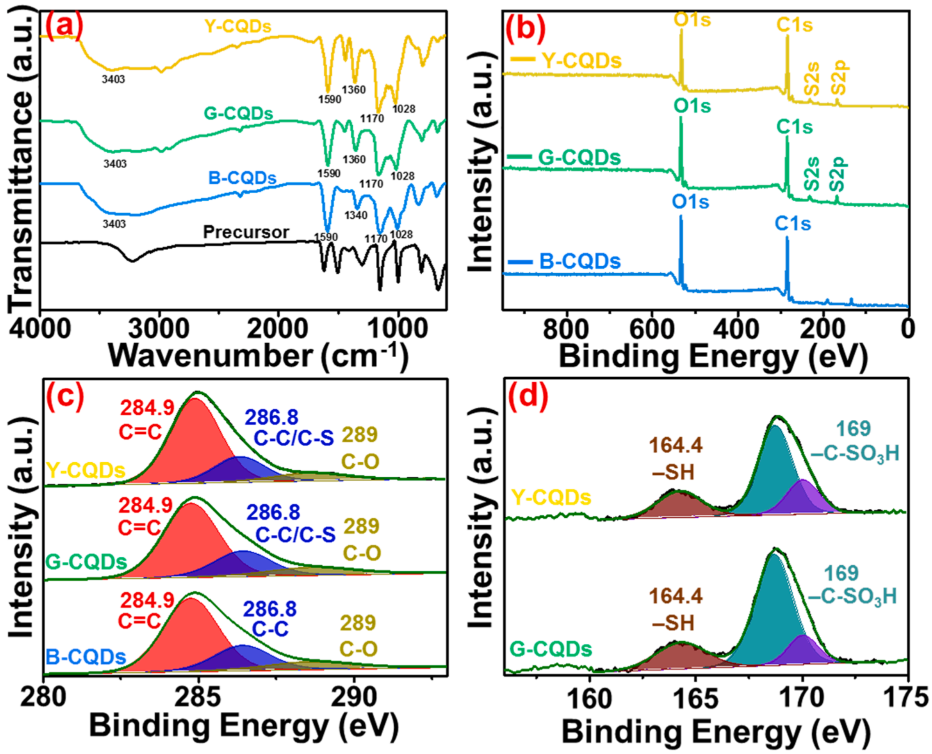

Fig. 4. (a) FT-IR spectra of precursor and CQDs; (b) XPS total survey spectra of B-CQDs, G-CQDs, and Y-CQDs; (c) high-resolution C1s XPS spectra; (d) high-resolution S2p XPS spectra.

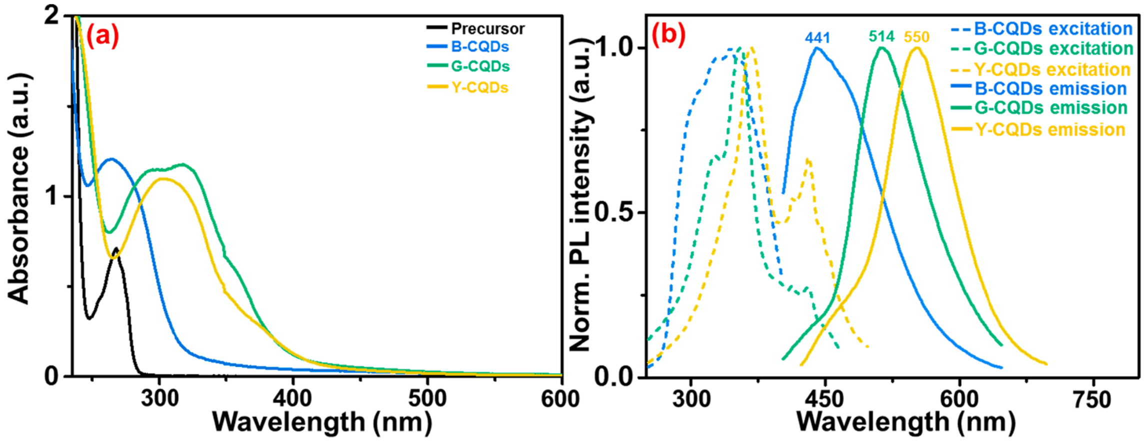

Fig. 5. (a) UV–vis absorption spectra of precursor and CQDs; (b) PL excitation and PL emission spectra of CQDs.

characteristic broad peaks may be assigned to the typical π–π* transition of the conjugated polyphenolic aromatic carbogenic core, hybridized with hydroxyl moieties [40,41]. The gradual bathochromic shift in the UV–Vis band from blue to yellow is in good agreement with the HR-TEM results, indicating the formation of larger dots with an increase in the sulfuric acid ratio. Furthermore, to gain more insight into the fluorescence (FL) properties, the PL emission spectra (Fig. 5**b)** of all the CQDs were recorded. The precursor itself did not have any FL emission property, but after thermal treatment, three distinct CQDs with blue, green, and yellow emissions were obtained, exhibiting PL emission maxima at approximately 441, 514, and 550 nm, respectively. Although there was a considerable bathochromic PL emission shift from B-CQDs to Y-CQDs in the range of 441–550 nm, the PL excitation spectra did not exhibit a significant shift. The PL excitation maxima (λ_{ex}) for B-, G-, and Y-CQDs were observed at 345, 355, and 365 nm, respectively. Similarly, UV–Vis absorption and PL emission spectra of CQDs prepared in various ratio mixtures (H_2SO_4: H_3PO_4 ratios (i) 0.4 mL: 1.6 mL, (ii) 0.8 mL: 1.2 mL, (iii) 1.2 mL: 0.8 mL, and (iv) 1.6 mL: 0.4 mL) are shown in **Fig. S7 (ESI†).** Significant efforts have been devoted to synthesizing multicolor CDs, and several strategies have been reported so far, as shown in Table 1. Our preparation method is based on the controllable acidic strength of the reaction using various ratio mixtures of sulfuric and phosphoric acid medium.

Furthermore, the bandgap energies of B-, G-, and Y-CQDs were determined using the equation $E_g^{opt} = 1240/\lambda$, where λ is the onset value of first excitonic absorption peaks in the direction of longer wavelengths. The bandgap energies of B-, G-, and Y-CQDs were calculated to be 3.91, 3.31, and 3.26 eV (**Fig. S8**, **ESI†**). The bandgap energies gradually decreased from 3.91 to 3.26 eV, which is in well accordance with the bathochromic shifting of PL emission spectra from 441 to 550 nm. To check the optical properties of products obtained from thermal heating of 1,3,5-trihydroxybenzene in closed system, we performed the

Table 1
Literature survey on the strategies for the synthesis of multicolor CQDs.

Materials	Strategy	Synthesis method	Presence of nitrogen	PL shift (nm)	Application	References
Diaminobenzene isomers	Selection of proper precursor	Solvothermal	Yes	Blue-435 Green-535 Red-604	Multicolor cellular imaging	[15]
Diaminonaphthalene isomers	Selection of proper precursor	Solvothermal	Yes	Blue Green Yellow Red	Multicolor bioimaging	[42]
Dihydroxybenzene isomers	Selection of proper precursor	Hydrothermal	Yes	Red-598Yellow-550 Green-518 Blue-417	No	[43]
Phloroglucinol	Chromatographic separation	Solvothermal	No	Blue-472 Green-507 Yellow-538 Red-598	Multicolored LEDs	[7]
Phloroglucinol	Reaction time monitor	Thermal heating	No	Blue-438 Green-512 Yellow-550	Multicolor bioimaging	[2]
1,3,6-trinitropyrene	Solvent engineering	Solvothermal	Yes	Blue-460 Green-517 Yellow-581 Red-620	Bioimaging	[9]
Citric acid and urea	Optimization of reagent ratio	Solvothermal	Yes	Blue-430 Green-540 Red-630	LEDs	[10]
1,2-diamino-4,5-difluorobenzene	Chemical doping	Solvothermal	Yes	Green-510 (undoped) Yellow-550 (F-doped) Orange-600 (F-doped)	Cell imaging and Ag^+ sensing	[11]
Citric acid and ethanolamine	Concentration variation	Hydrothermal	Yes	430–617 Blue-Red	W-LEDs for solid state lightening	[14]
p-phenylenediamine	Solvatochromism	Thermal heating in reflux condenser followed by quick inject	Yes	Green-511 Yellow-554 Red-602	Solid state films for color displays	[8]
Carbon particles	Surface passivation	Nitric acid treatment followed by surface passivation with PEG_{1500N}	Yes	Blue-450 Green-500 Yellow-550 Red-650	Bioimaging	[6]
Citric acid and urea	Temperature-control	Solvothermal	Yes	Blue-470 Yellow-546 Orange-Red-585	Polymer films for LEDs	[44]
Galactose and cysteine	pH controlled synthesis under alkaline condition	Reflux method using Maillard reaction condition	Yes	Blue-400 Green-515 Yellow-550	Detection of caffeine, melamine, fenitrothion	[12]
1,3,5-trihydroxybenzene	Acid strength tuning (different ratiometric mixtures of sulfuric acid: phosphoric acid)	Thermal heating at 190 °C for 90 min	No	Blue-441 Green-514 Yellow-550	Multicolor bioimaging NIR-responsive photothermal antibacterial activity	This work

synthesis using poly(tetrafluoroethylene)-lined autoclave keeping the reaction condition unaltered for 90 min at 190 °C. Interestingly, we didn't get multicolor CQDs rather we only observed blue emissive products with UV–vis absorption at 262 nm and PL emission maxima $\lambda_{em} = 460$ nm under the excitation of 350 nm. The corresponding UV–vis spectra and PL emission spectra are detailed in Fig. S9 **(ESI†).** Furthermore, the CQDs were excited at various wavelengths to verify the excitation-dependent emission behavior. Excitation-dependent emission properties were observed, with maximal values at excitations of 345, 355, and 365 nm for B-, G-, and Y-CQDs, respectively, as shown in Fig. S10 **(ESI†).** To obtain deeper insights into the optical characteristics, the absolute QY **(**Fig. S11**a, ESI†)** was evaluated using a comparative approach taking quinine sulfate (QY: 54 % in 0.1 M H_2SO_4) as reference standard. The experimental details have been provided in Section 2.1 **(ESI†).** The absolute QY for the B-, G-, and Y-CQDs in ethanol was calculated to be 3.26, 27%, and 8.34%, respectively. Furthermore, the QY yield of G-, and Y-CQDs were measured in aqueous media containing 0.5% ethanol (experimental media) and the values are calculated to be 8.8% and 2.4%, respectively as shown in **(**Fig. S11**b) (ESI†).** Although the quantum yield values are comparatively lower in the experimental aqueous media with respect to ethanolic solution due to lower dispersibility, yet enough to be used for biological experiments. Finally, to assess the NIR light responsive photophysical properties, we recorded Vis-NIR absorption and excitation spectra in the Vis-NIR range from 600 to 1000 nm, as shown in Fig. S12**a & b (ESI†).** The Vis-NIR absorption spectra exhibited that Y-CQDs (200 μg/mL) have a broad range of optical absorption (600–1000 nm) in the NIR-range. Similarly, the excitation spectra of Y-CQDs (200 μg/mL) displayed broad excitation band in the range of 800–900 nm. Fig. S12**c & d (ESI†)** shows the PL emission spectra at various excitation wavelength (600 to 900 nm) for G-, and Y-CQDs, respectively. It was observed that both the CQDs had high emission under the excitation of Vis-NIR light. Thus, the result indicates that CQDs contain continuous energy bands and at the excitation of 808 nm NIR-laser, both the CQDs sample is highly excited which implies their NIR-light absorption property.

3.5. Multicolor bioimaging and cellular uptake study

The as-prepared multicolor CQDs were used as propitious probes for multicolor cellular imaging because of their good photostability and excellent intercellular distribution. The in vitro cytotoxicity of all three distinct CQDs on human dermal fibroblast (hDFs) cells was evaluated using the WST-1 (EZ Cytox Cell Viability Assay Kit®, DoGen Bio, Republic of Korea) assay, as shown in Fig. S13a **(ESI†)**. The detailed experimental conditions for the in vitro biocompatibility assay are discussed in the **Section 2.2 (ESI†).** All CQDs were highly biocompatible with respect to hDFs cells, even after treatment with concentrations as high as 200 μg mL^{-1}. Furthermore, to evaluate the effect of all CQDs on red blood cells (RBCs), we performed a hemocompatibility assay **(**Fig. S13**b, ESI†)** in whole blood collected from BALB/c nude mice. The details for the experimental conditions are depicted in **Section 2.3 (ESI†)**. B-, G-, and Y-CQDs had excellent blood biocompatibility compared to the positive control group. Thus, all CQDs are promising probes for in vitro as well as in vivo bioimaging applications owing to their biocompatibility and limited toxicity.

To demonstrate the bioimaging potentials of B-, G-, and Y-CQDs, HepG2 cells were incubated with the three distinct CQDs individually, followed by imaging under FL microscopy. The cell imaging experimental conditions are detailed in **Section 2.4 (ESI†)**. The multicolor FL microscopy images with high cellular FL intensity of HepG2 cells

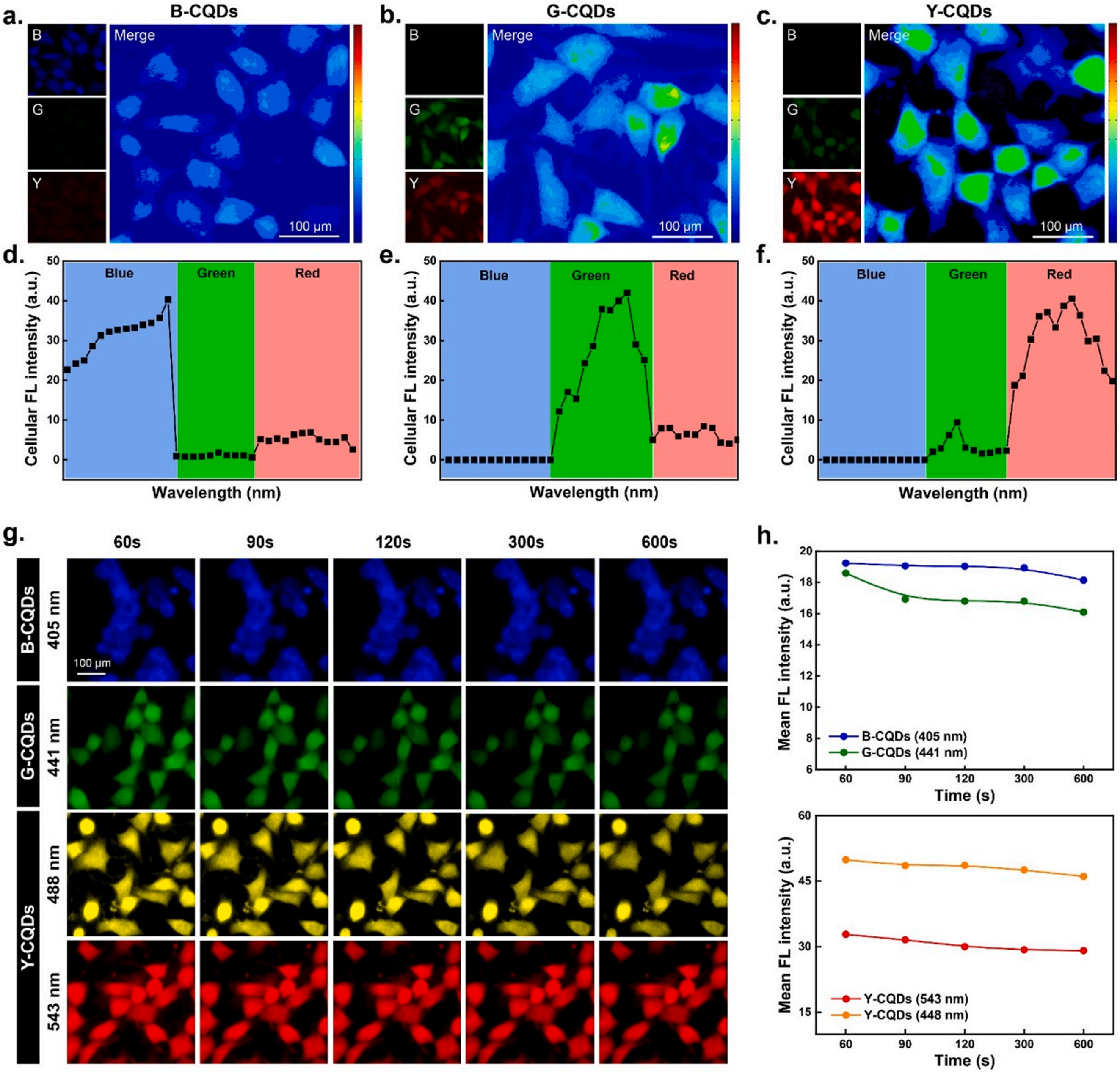

Fig. 6. Multicolor bioimaging property of CQDs. Representative LCSM and pseudo-color merge images of HepG2 cells incubated with (a) B-CQDs, (b) G-CQDs, and (c) Y-CQDs for 4 h. Images were taken with 405 nm, 441, and 543 nm excitation lasers for each CQDs. The color map indicates the maximum (red) and minimum (blue) pixel densities of the merge image. (d-f) Representative cellular FL intensity of B-CQDs, G-CQDs, and Y-CQDs at different excitations. (e) Photostability of B-CQDs, G-CQDs, and Y-CQDs at different excitation lasers for 10 min with (f) corresponding FL intensities. Scale bar: 100 μm.

incubated with B-, G-, and Y-CQDs (200 μg mL^{-1}) are shown in Fig. 6, displaying blue (B-CQDs), green (G-CQDs), yellow (Y-CQDs), and red (Y-CQDs) emissions under different laser channels of 405, 441, 448, and 543 nm, respectively. (Fig. 6**a, b), and c** show the merged images of the target cells incubated with B-, G-, and Y-CQDs, respectively. The predominant FL emission intensities of B-, G-, and Y-CQD-treated cells under various excitation channels were measured, as shown in (Fig. 6**d, e, and f),** respectively. (Fig. 6**g)** displays the photostability of B-, G-, and Y-CQDs under continuous irradiation for 10 min under FL microscopy, demonstrating excellent photostability with multicolor imaging capability under various excitation channels. This was also verified by measuring the FL intensities at different time intervals, as shown in (Fig. 6**h).**

Next, we investigated the cellular uptake of CQDs to verify multicolor imaging capability. Interestingly, the CQDs were predominantly up taken by the cells, as can be seen from the laser confocal scanning microscopy (LCSM) images **(Fig. S14, ESI†)** when incubated under confocal microscopy, making them an excellent imaging probe. These findings were identical to those observed in previous reports [45]. Furthermore, we examined the lysosomal delivery efficiency of the CQDs. For this, the cells were incubated with various CQDs (50 μg mL^{-1}) for different time points and stained with LysoTracker Red (Abcam, USA). Images were taken using an inverted FL microscope, and the results are shown in Fig. 7. Cells without CQD treatment were used as control sets. As shown in (Fig. 7**a)**, the control cells exhibited bright red cytoplasmic patches, indicating the presence of lysosomes. However, in CQD-treated cells, a dramatic change in lysosomal FL was observed. Before 1 h, the cells exhibited clear lysosomal staining and CQD localization, demonstrating that CQD delivery was mediated through lysosomes. However, after 1 h, the lysosomal FL drastically decreased. In G-CQDs and Y-CQDs-treated cells, lysosomal FL completely disappeared, as shown in (Fig. 7**c and d)**. The B-CQD-treated cells **(**Fig. 7**b)** showed negligible FL after 2 h of incubation. This can be explained by the excess accumulation of CQDs inside the lysosomal vesicles and rapid quenching of LysoTracker Red by a mechanism known as FL resonance energy transfer or π-π stacking, as reported earlier for various fluorescent dyes [4,46–49].

3.6. NIR-responsive photothermal properties

The NIR-responsive photothermal performance of all CQDs was investigated by irradiating them with NIR light of 808-nm wavelength, with water as the control. The experimental conditions for the photothermal performance of CQDs and measurement of photothermal conversion efficiency are discussed in **Sections 2.5 and 2.6 (ESI†)**, respectively. The temperature change as a function of time was recorded

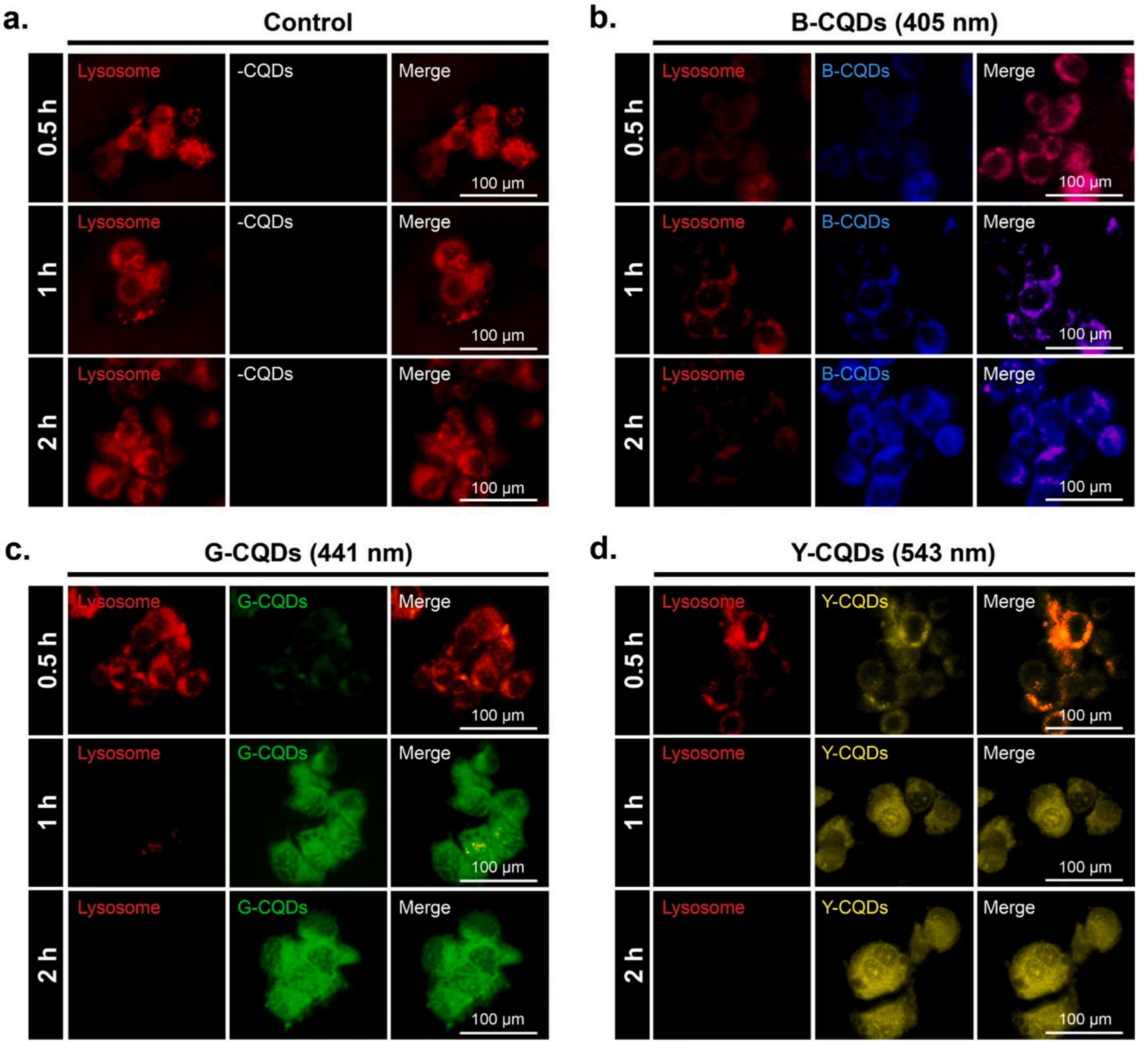

Fig. 7. Fluorescence microscopy images indicating the sub-cellular distribution (a) without CQDs, (b) with B-CQDs, (c) with G-CQDs, and (d) with Y-CQDs. All images were captured with appropriate excitation. LysoTracker deep red was used to stain the lysosomes to investigate the lysosomal delivery of CQDs. Scale bar: 100 μm.

for each CQDs with different concentrations (25 to 200 μg/mL) under constant laser power stimulation (1 W/cm^2). (Fig. 8**a, 8b, and 8c)** shows the temperature increase profile of different CQDs with various concentrations as a function of time under NIR laser (808 nm, 1 W/cm^2) irradiation. Notably, with increasing concentration of CQDs, a gradual increase in temperature was observed. The B-CQDs showed a slight increase in temperature as the concentration increased from 25 to 200 μg/mL (Fig. 8**a**). The temperature-NIR irradiation time curve of B-CQDs dispersed in water exhibited a gradual rise in temperature from 28 °C to 45 °C after 5 min of irradiation, whereas no significant change in temperature was detected for the control sample (water). Initially, at a low concentration (25 μg/mL), there was no significant increase in the temperature of the B-CQDs. However, at a higher concentration (200 μg/mL), a slight increase was observed. The photothermal activity was strongly dependent on the concentration of the CQDs; thus, a higher content of CQDs in water resulted in a higher temperature rise, probably due to the higher amount of NIR absorption at 808 nm [33,50,51]. More specifically, for Y-CQDs contents of 25, 50, 100, and 200 μg/mL, the rise in temperature was 57, 63, 69, and 73 °C, respectively (Fig. 8**c**), indicating that Y-CQDs have excellent photothermal performance, making them suitable for antibacterial applications with photothermal therapy. Moreover, the concentration dependent temperature change (ΔT) over a period 360 s of the B-, G-, and Y-CQDs are given in (Fig. 8**d, 8e, and 8f).** The experimental results showed that G-, and Y-CQDs at a rather low concentration (200 μg/mL) can efficiently transform the NIR laser energy into thermal energy. (Fig. 8**g, 8 h, and 8i)** shows the plot of cooling time versus negative natural logarithm of the temperature driving force obtained from cooling period. The time constant τ_s for heat transfer of the system was determined to be 122.62, 155.51, and 171.46 s for B-, G-, and Y-CQDs, respectively. (Fig. 9**a)** shows the NIR thermal images of B-, G-, and Y-CQDs aqueous solutions at different time interval, which further verified the conversion of photo-energy to thermal energy. The photothermal conversion efficiency **(**Fig. 9**b)** was determined to be 10.8 ± 0.5%, 22.7 ± 1%, and 32.6 ± 1% for B-, G-, and Y-CQDs, respectively. The comparison table for the photothermal efficiency of CDs reported previously are provided in Table 2.

Moreover, the photothermal stability **(**Fig. 9**c, 9d, and 9e)** of B-, G-, and Y-CQDs (200 μg/mL) showed excellent photostability over eight on/off cycles of 808-nm laser light at 1 W/cm^2 power density. It is to be noted that both G-, and Y-CQDs have more or less same photothermal activity with Y-CQDs slightly higher. Both G- and Y-CQDs exhibited higher photothermal efficiency compared to B-CQDs, probably because of the larger size of the particles and, consequently, better absorption of NIR. It was discussed earlier that sulfuric acid, as a very strong

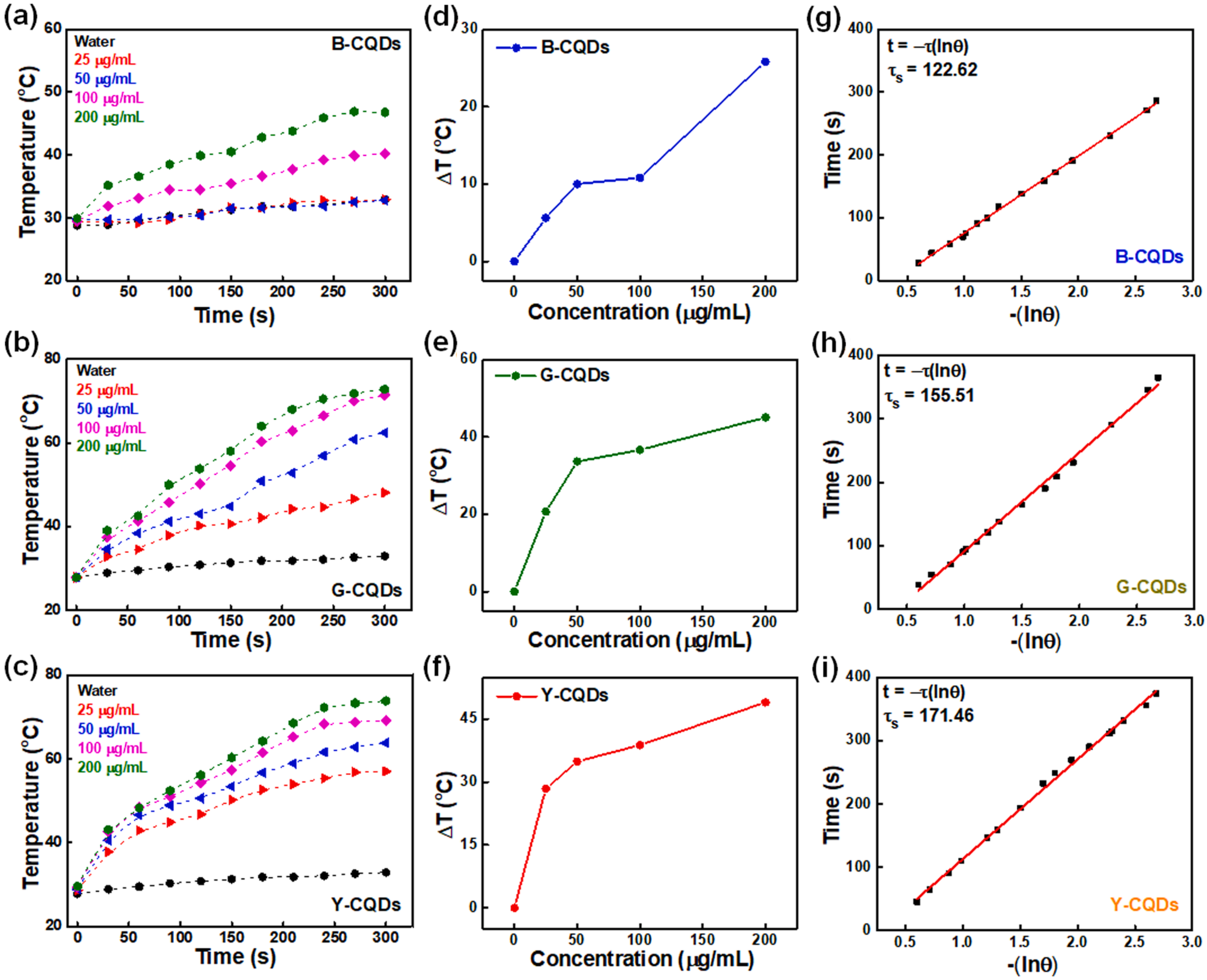

Fig. 8. Photothermal conversion of CQDs. (a, b, c) Temperature increase profile of the different CQDs with various concentrations as a function of time under NIR laser (808 nm, 1 W/cm^2) irradiation. (d, e, f) Plot of temperature change (ΔT) over a period of 300 s versus different concentrations of B-, G-, Y-CQDs. (g, h, i) Plot of cooling time versus negative natural logarithm of the temperature driving force obtained from the cooling period.

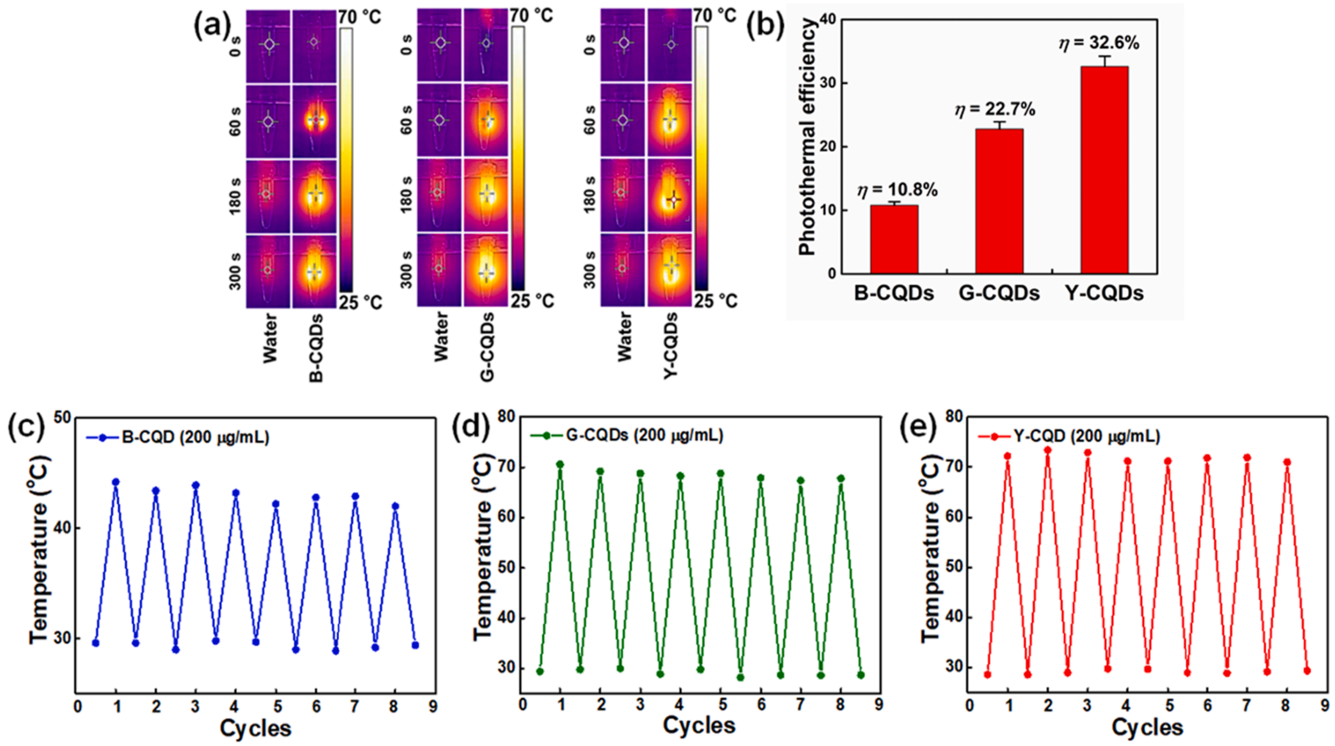

Fig. 9. (a) IR images of water and aqueous CQDs solutions under 808 nm laser (1 W/cm^2) irradiation for different time intervals. (b) photothermal conversion efficiency of B-, G-, and Y-CQDs [experimental errors for PCE: B-CQDs (10.8 ± 0.5%), G-CQDs (22.7 ± 1%), and Y-CQDs (32.6 ± 1%)]; (c, d, e) Temperature variation of the CQDs (200 μg/mL) over eight on/off cycles of 808-nm laser light at 1 W/cm^2 power density.

Table 2
The comparison table for the photothermal conversion efficiency of CDs reported previously in the literature.

CQDs precursor	Dose (μg/mL)	Power density (W/cm^2)	Laser(nm)	Irradiation time (min)	Efficiency (%)	References
Citric acid and oleylamine	2×10^4	2	808	10	3.77	[52]
polythiophene benzoic acid	200	2	635	10	36.2	[53]
Polythiophene and diphenyl diselenide	10^3	2	635	10	58.2	[54]
citric acid and dicyandiamide	10^4	4	808	10	41.7	[55]
cyanine dye and PEG800	125	2	808	10	38.7	[56]
Dopamine hydrochloride	50	1.5	808	5	35	[57]
nitro-coronene derivative	200	2	808	10	54.7	[58]
Citric acid and urea	45×10^4	1.2	655	10	54.3	[59]
Citric acid and urea	200	1	655	10	59.2	[60]
Hypocrella bambusae	200	0.8	635	10	27.6	[61]
watermelon juice	2×10^4	1.4	808	10	30.6	[62]
1,3,5-trihydroxybenzene	200	1	808	5	B-CQDs-10.8 ± 0.5 G-CQDs-22.7 ± 1 Y-CQDs-32.6 ± 1	This work

dehydrating acid, can engage in the formation of CQDs with larger conjugated domain and graphene-oxide like particles compared to phosphoric acid.

3.7. In vitro hyperthermia-induced antibacterial activity

The outstanding photothermal efficiency of the CQDs motivated us to scrutinize its antibacterial properties in vitro. Hyperthermia-induced membrane damage and high reactive oxygen species (ROS) amplification are key mechanisms of bacterial killing [63]. The NIR-responsive photothermal antibacterial efficacy of all CQDs was investigated against *Bacillus subtilis* with and without NIR laser irradiation. The in vitro antimicrobial effects of the as-prepared CQDs were evaluated in terms of the liquid culture method, plate dilution method, live-dead assay, morphological observations, and ROS generation, and the corresponding experimental details are discussed in **Section 2.7. (1–5)** **[(ESI†)]**. The results of relative viability without NIR treatment (Fig. 10**a)** of *Bacillus subtilis* demonstrate the antibacterial performance of all the CQDs, which reveals that all the CQDs have mild antibacterial effects due to their inherent nature. The order of effectiveness increased as the size of the particles increased. Moreover, the time-dependent treatment showed that the relative viability decreased gradually with time, implying that CQDs were toxic to bacteria over the duration of exposure. After 24 h of exposure time, the killing ratio reached almost 45%, 50%, and 55% for B-, G-, and Y-CQDs, respectively. In contrast, the relative viability of *Bacillus subtilis* decreased significantly after 5 min of NIR irradiation, as shown in (Fig. 10**b)**. The NIR-treated (5 min) sample exhibited killing ratios of up to 55%, 90%, and 95 % after 24 h for B-, G-, and Y-CQDs, respectively. The order of photothermal antibacterial efficacy increased with the size of the particles, probably due to the higher absorption of NIR radiation, and the results were in good agreement with the photothermal efficiency. Furthermore, to validate the impact of

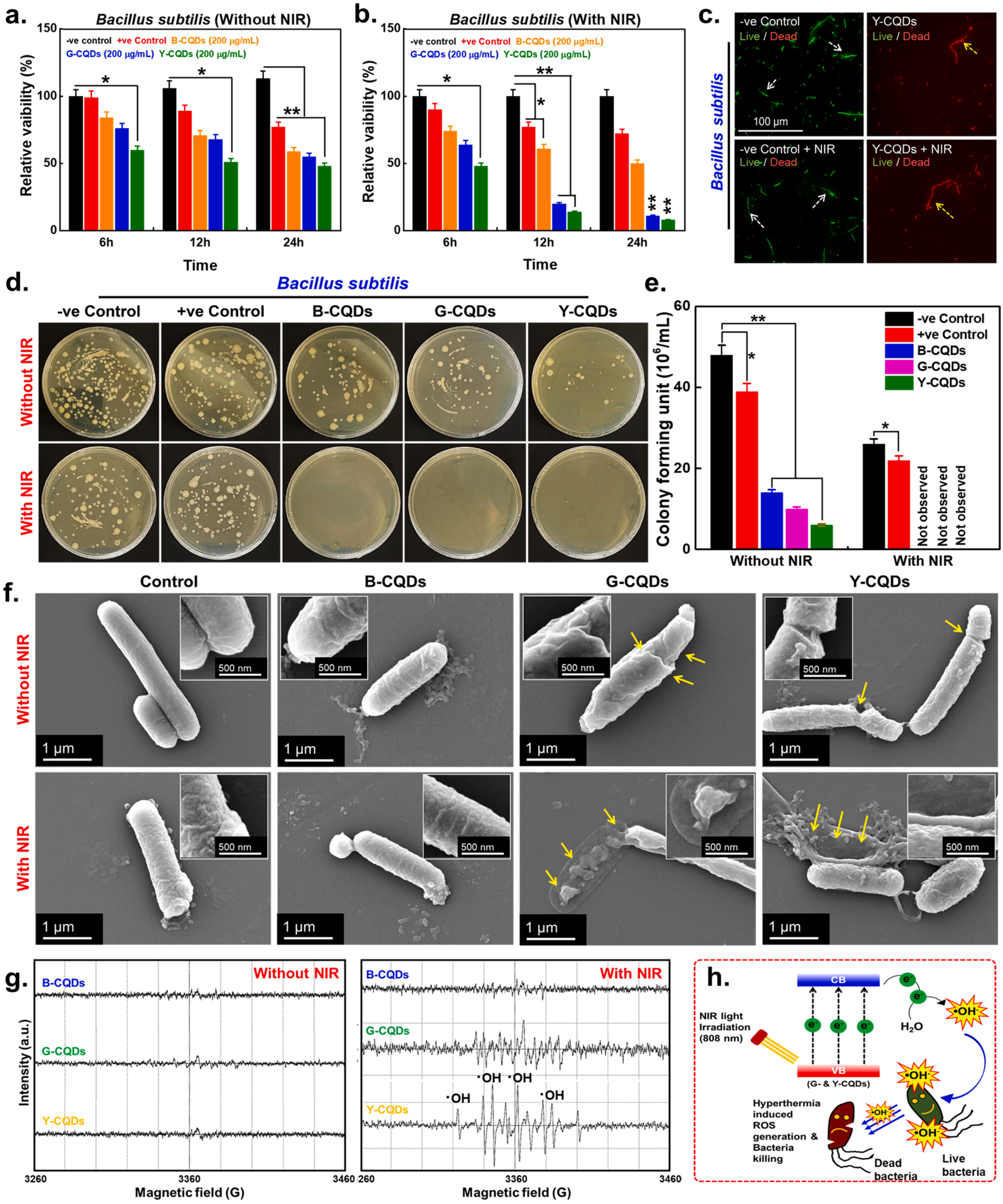

Fig. 10. Anti-bacterial performance of CQDs. (a-b) Relative viability of *Bacillus subtilis* with and without NIR light (808 nm) irradiation (1 W/cm) at indicated time intervals. (c) Live-dead assay indicating the bacterial viability. Scale bar: 100 μm. (d) Agar plate counting method for *B. subtilis* with and without NIR irradiation after 24 h of culture in NA media. PBS and DMSO were taken as negative and positive control groups, respectively. (e) Colony forming unit as quantified by ImageJ software. (f) Evaluation of bacterial morphology by HR-SEM. Scale bar: 500 nm and 1 μm (×25,000 and × 50,000 magnification). DM; damaged membrane. Data are mean ± s.d. (n = 3), statistical significance at $*p < 0.05$ and $*p < 0.01$ (Student *t*-test). (g) ESR spectra of the CQDs sample exhibiting characteristic signals of $^{\bullet}$OH radicals in presence of NIR light (808 nm, 1 W/cm^2). (h) Schematic illustration for the mechanism of bactericidal activity of the CQDs.

NIR radiation on the antibacterial property, a live-dead assay **(**Fig. 10**c)** was performed by FL staining of the sample after NIR treatment. Specifically, a nucleic acid stain (acridine orange) was labeled with live *Bacillus subtilis* producing green FL, whereas dead *Bacillus subtilis* was labeled with ethidium bromide, which displays orange-red FL due to damage to the cellular membrane. As shown in (Fig. 10**c)**, bacteria showed bright green FL in phosphate buffered saline (PBS) with and without NIR treatment, whereas the CQD-treated sample showed red FL, which further intensified after NIR treatment resulting from disruption of the cytoplasmic membrane and induced cell death. This result was further confirmed by the agar plate counting method for *Bacillus subtilis* with and without NIR irradiation after 24 h of culture in nutrient agar (NA) media, where PBS and dimethyl sulfoxide (DMSO) were used as negative and positive control groups, respectively. The agar plate assay **(**Fig. 10**d)** clearly demonstrated the impact of CQDs and (CQDs + NIR) treatments on bacterial cells. Bacterial colony forming capability decreased after CQDs treatment, as evidenced by a decrease in density. The Y-CQDs exhibited the superior antibacterial performance compared to the others. After NIR irradiation for 6 min, bacterial growth was restricted, and no colony formation observed as shown by colony formation efficiency **(**Fig. 10**e)**. In addition, we recorded high resolution images in scanning electron microscopy (SEM) to inspect the morphology of the bacterial cells, as shown in (Fig. 10**f)**. SEM images of bacterial cells incubated with PBS clearly displayed intact bacterial cells with and without NIR irradiation in the absence of CQDs. After Y-CQDs treatment, *Bacillus subtilis* cell membranes started to rupture and the process intensified with NIR treatment, which completely damaged the cytoplasmic membrane. **Fig. S15 (ESI†)** exhibits the representative FE-SEM images of the B. subtilis colony (5 μm scale bar) after irradiated with or without NIR laser in the presence of Y-CQDs. The Y-CQDs exhibited serious membrane damage in the bacteria followed by leakage of the cellular components. **Fig. S16 (ESI†)** shows the representative HR-SEM images of a single B. subtilis bacterium (at 1 μm scale bar) after irradiated with NIR laser in the presence of Y-CQDs showing (a) Leakage of cellular components, and (b) rupture of the cell membrane. Thus, based on the above experimental results, CQDs demonstrated excellent potential to inhibit bacterial infections owing to their NIR-induced photothermal activation properties.

To gain more insight into the antibacterial mechanism, we performed the electron spin resonance (ESR) spectra to identify the ROS production with and without NIR light irradiation. Polyphenolic compounds derived CQDs are much more prone to produce huge amount of hydroxyl ($^{\bullet}$OH) radical under external light stimuli. So, to determine the production of ROS, we recorded the ESR spectra with 5,5-dimethyl-1-pyrroline N-oxide (DMPO) as a trapping agent for $^{\bullet}$OH radicals in DI water. (Fig. 10**g)** shows the ESR spectra of B-, G-, and Y-CQDs with and without the presence of NIR light. It is to be noted that under the dark condition, no ESR signals were detected, whereas multiple signals were observed under NIR irradiation corresponding to the $^{\bullet}$OH radicals. Y-CQDs exhibited sharp characteristic peaks with an intensity ratio of 1:2:2:1 corresponding to $^{\bullet}$OH radicals [64,65]. ESR peaks due to $^{\bullet}$OH radicals are most prominent in Y-CQDs compared to G-, and B-CQDs, making it an ideal photothermal agent for antibacterial application through radical pathways in co-operation with hyperthermia effect. Based on the NIR-induced generation of $^{\bullet}$OH radicals, a plausible mechanism of bactericidal activity has been drawn (Fig. 10*h*).

To gain more insight into the bacterial killing mechanism, dichlorodihydrofluorescein diacetate (DCFDA) staining was performed. Briefly, the bacterial cells were incubated with various formulations of CQDs with and without NIR irradiation for 24 h. After that, the cells were incubated with the ROS-sensitive probe DCFDA, and the FL intensity was measured at $^{ex}/_{em}$ of $^{485}/_{528}$ nm. As shown in **Fig. S17 (ESI†)**, the bacterial cells exhibited a significant increase in ROS generation in the presence of NIR irradiation for 6 min compared to the untreated groups. The ROS generations in the NIR-irradiated B-CQDs, G-CQDs, and Y-CQDs-treated cells were 128%, 150%, and 188%, respectively, which were considerably higher than those in the control groups. CQDs are known to alter the microenvironments of bacteria by interacting with respiratory enzymes, DNA metabolism, and membrane ion transport [63,66]. Considered together, our results demonstrate that hyperthermia-induced bactericidal activity is due to elevated ROS amplification and membrane damage of *Bacillus subtilis*.

4. Conclusion

In this study, a strategy was proposed to synthesize PL-emission-tunable multicolor CQDs based on controllable acidic strength using a wet chemistry-based synthetic approach. Multicolor CQDs were obtained from 1,3,5-trihydroxybenzene through a facile thermal heating process in the reaction medium of different ratiometric mixtures of sulfuric and phosphoric acids (S: P) under 90 min of reaction at 190 °C. Multicolor emissive CQDs have been utilized as promising luminous probes for multicolor cellular imaging because of their good biocompatibility and effective intracellular distribution. Moreover, the as-prepared CQDs exhibited a high photothermal conversion efficiency of NIR light energy (808 nm) into thermal energy, and thus exhibited remarkable photothermal bactericidal activity compared to CQDs alone (which also have considerable antibacterial activity) via ROS generation and membrane damage. Y-CQDs with larger polyaromatic sp^2 domains and higher oxidized surfaces exhibited a high photothermal conversion efficiency (PCE ~ 32.6 ± 1%) and thus exhibited remarkable NIR-light responsive photothermal bactericidal activity. Our results demonstrate that hyperthermia-induced bactericidal activity is due to the elevated reactive oxygen species (ROS) amplification and membrane damage of *Bacillus subtilis*. This study provides a potential application of CQDs for the multicolor imaging guided phototherapy.

CRediT authorship contribution statement

Md Moniruzzaman: Conceptualization, Investigation, Methodology, Data curation, Formal analysis, Writing – original draft. **Sayan Deb Dutta:** Conceptualization, Investigation, Methodology, Data curation, Formal analysis, Writing – original draft. **Ki-Taek Lim:** Supervision, Validation, Funding acquisition, Project administration, Writing – review & editing. **Jongsung Kim:** Supervision, Validation, Funding acquisition, Project administration, Writing – review & editing.

Declaration of Competing Interest

The authors declare that they have no known competing financial interests or personal relationships that could have appeared to influence the work reported in this paper.

Acknowledgements

This research was supported by the Basic Science Research Program through the National Research Foundation of Korea (NRF) funded by the Ministry of Education (Grant No.-2021R1A6A1A03038996). This work was also supported by the 'Basic Research Program' through the 'National Research Foundation of Korea (NRF)' funded by the 'Ministry of Education (Grant No.-2018R1A6A1A03025582 & 2019R1D1A3A03103828). The authors also acknowledge the Smart Materials Research Center for IoT, Gachon University, for its kind help in XRD and FT-IR analysis. We would also like to thank the Korea Basic Science Institute (KBSI), Chuncheon Center for the HR-SEM facility.

Appendix A. Supplementary material

Supplementary data to this article can be found online at https://doi.org/10.1016/j.apsusc.2022.153630.

References

[1] M.d. Moniruzzaman, J. Kim, N-doped carbon dots with tunable emission for multifaceted application: solvatochromism, moisture sensing, pH sensing, and solid state multicolor lighting, Sens. Actuators, B 295 (2019) 12–21.

[2] M.d. Moniruzzaman, B. Anantha Lakshmi, S. Kim, J. Kim, Preparation of shape-specific (trilateral and quadrilateral) carbon quantum dots towards multiple color emission, Nanoscale. 12 (22) (2020) 11947–11959.

[3] F. Yuan, Z. Wang, X. Li, Y. Li, Z. Tan, L. Fan, S. Yang, Bright multicolor bandgap fluorescent carbon quantum dots for electroluminescent light-Emitting diodes, Adv. Mater. 29 (3) (2017) 1604436, https://doi.org/10.1002/adma.v29.310.1002/adma.201604436.

[4] M.d. Moniruzzaman, J. Kim, Shape-engineered carbon quantum dots embedded on CdS-nanorods for enhanced visible light harvesting towards photocatalytic application, Appl. Surf. Sci. 552 (2021) 149372, https://doi.org/10.1016/j.apsusc.2021.149372.

[5] K. Jiang, S. Sun, L. Zhang, Y. Wang, C. Cai, H. Lin, Bright-yellow-emissive N-doped carbon dots: preparation, cellular imaging, and bifunctional sensing, ACS Appl. Mater. Interfaces 7 (41) (2015) 23231–23238.

[6] Y.-P. Sun, B. Zhou, Y.i. Lin, W. Wang, K.A.S. Fernando, P. Pathak, M.J. Meziani, B. A. Harruff, X. Wang, H. Wang, P.G. Luo, H. Yang, M.E. Kose, B. Chen, L.M. Veca, S.-Y. Xie, Quantum-sized carbon dots for bright and colorful photoluminescence, J. Am. Chem. Soc. 128 (24) (2006) 7756–7757.

[7] F. Yuan, T. Yuan, L. Sui, Z. Wang, Z. Xi, Y. Li, X. Li, L. Fan, Z. Tan, A. Chen, M. Jin, S. Yang, Engineering triangular carbon quantum dots with unprecedented narrow bandwidth emission for multicolored LEDs, Nat. Commun. 9 (1) (2018), https://doi.org/10.1038/s41467-018-04635-5.

[8] H. Wang, C. Sun, X. Chen, Y.u. Zhang, V.L. Colvin, Q. Rice, J. Seo, S. Feng, S. Wang, W.W. Yu, Excitation wavelength independent visible color emission of carbon dots, Nanoscale. 9 (5) (2017) 1909–1915.

[9] J. Zhan, B. Geng, K. Wu, G. Xu, L. Wang, R. Guo, B.o. Lei, F. Zheng, D. Pan, M. Wu, A solvent-engineered molecule fusion strategy for rational synthesis of carbon quantum dots with multicolor bandgap fluorescence, Carbon 130 (2018) 153–163.

[10] X. Miao, D. Qu, D. Yang, B. Nie, Y. Zhao, H. Fan, Z. Sun, Synthesis of carbon dots with multiple color emission by controlled graphitization and surface functionalization, Adv. Mater. 30 (1) (2018) 1704740, https://doi.org/10.1002/adma.v30.110.1002/adma.201704740.

[11] G. Zuo, A. Xie, J. Li, T. Su, X. Pan, W. Dong, Large emission red-shift of carbon dots by fluorine doping and their applications for red cell imaging and sensitive intracellular Ag+ detection, The Journal of Physical Chemistry C. 121 (47) (2017) 26558–26565.

[12] T.-Y. Wang, C.-Y. Chen, C.-M. Wang, Y.Z. Tan, W.-S. Liao, Multicolor functional carbon dots via one-step refluxing synthesis, ACS Sensors 2 (3) (2017) 354–363.

[13] S. Chung, R.A. Revia, M. Zhang, Graphene quantum dots and their applications in bioimaging, biosensing, and therapy, Adv. Mater. 33 (22) (2021) 1904362, https://doi.org/10.1002/adma.v33.2210.1002/adma.201904362.

[14] Y. Chen, H. Lian, Y.i. Wei, X. He, Y. Chen, B.o. Wang, Q. Zeng, J. Lin, Concentration-induced multi-colored emissions in carbon dots: origination from triple fluorescent centers, Nanoscale. 10 (14) (2018) 6734–6743.

[15] K. Jiang, S. Sun, L. Zhang, Y. Lu, A. Wu, C. Cai, H. Lin, Red, green, and blue luminescence by carbon dots: full-color emission tuning and multicolor cellular imaging, Angew. Chem. 127 (18) (2015) 5450–5453.

[16] Y. Yan, L. Xia, L. Ma, Solvent-controlled synthesis of multicolor photoluminescent carbon dots for bioimaging, RSC Adv. 9 (42) (2019) 24057–24065.

[17] H. Ding, S.-B. Yu, J.-S. Wei, H.-M. Xiong, Full-color light-emitting carbon dots with a surface-state-controlled luminescence mechanism, ACS Nano 10 (1) (2016) 484–491.

[18] H. Ding, J.-S. Wei, P. Zhang, Z.-Y. Zhou, Q.-Y. Gao, H.-M. Xiong, Solvent-controlled synthesis of highly luminescent carbon dots with a wide color gamut and narrowed emission peak widths, Small. 14 (22) (2018) 1800612, https://doi.org/10.1002/smll.v14.2210.1002/smll.201800612.

[19] C. Liu, Y. Jin, R. Wang, T. Han, X. Liu, B. Wang, C. Huang, S. Zhu, J. Chen, Indole carbonized polymer dots boost full-color emission by regulating surface state, Iscience. 23 (10) (2020) 101546, https://doi.org/10.1016/j.isci.2020.101546.

[20] L. Guo, J. Ge, W. Liu, G. Niu, Q. Jia, H. Wang, P. Wang, Tunable multicolor carbon dots prepared from well-defined polythiophene derivatives and their emission mechanism, Nanoscale. 8 (2) (2016) 729–734.

[21] Y. Zhang, R. Yuan, M. He, G. Hu, J. Jiang, T. Xu, L. Zhou, W. Chen, W. Xiang, X. Liang, Multicolour nitrogen-doped carbon dots: tunable photoluminescence and sandwich fluorescent glass-based light-emitting diodes, Nanoscale. 9 (45) (2017) 17849–17858.

[22] W. Li, Z. Zhang, B. Kong, S. Feng, J. Wang, L. Wang, J. Yang, F. Zhang, P. Wu, D. Zhao, Simple and green synthesis of nitrogen-doped photoluminescent carbonaceous nanospheres for bioimaging, Angew. Chem. Int. Ed. 52 (31) (2013) 8151–8155.

[23] S. Zhu, J. Zhang, C. Qiao, S. Tang, Y. Li, W. Yuan, B.o. Li, L.u. Tian, F. Liu, R. Hu, H. Gao, H. Wei, H. Zhang, H. Sun, B. Yang, Strongly green-photoluminescent graphene quantum dots for bioimaging applications, Chem. Commun. 47 (24) (2011) 6858, https://doi.org/10.1039/c1cc11122a.

[24] L. Pan, S. Sun, A. Zhang, K. Jiang, L. Zhang, C. Dong, Q. Huang, A. Wu, H. Lin, Truly fluorescent excitation-dependent carbon dots and their applications in multicolor cellular imaging and multidimensional sensing, Adv. Mater. 27 (47) (2015) 7782–7787.

[25] L. Feng, L. Liu, F. Lv, G.C. Bazan, S. Wang, Preparation and biofunctionalization of multicolor conjugated polymer nanoparticles for imaging and detection of tumor cells, Adv. Mater. 26 (23) (2014) 3926–3930.

[26] Y. Ren, H. Liu, X. Liu, Y. Zheng, Z. Li, C. Li, K.W.K. Yeung, S. Zhu, Y. Liang, Z. Cui, S. Wu, Photoresponsive materials for antibacterial applications. Cell Reports Physical, Science 1 (11) (2020) 100245, https://doi.org/10.1016/j.xcrp.2020.100245.

[27] Y. Qiao, F. Ma, C. Liu, B.o. Zhou, Q. Wei, W. Li, D. Zhong, Y. Li, M. Zhou, Near-infrared laser-excited nanoparticles to eradicate multidrug-resistant bacteria and promote wound healing, ACS Appl. Mater. Interfaces 10 (1) (2018) 193–206.

[28] M.u. Li, X. Liu, L. Tan, Z. Cui, X. Yang, Z. Li, Y. Zheng, K.W.K. Yeung, P.K. Chu, S. Wu, Noninvasive rapid bacteria-killing and acceleration of wound healing through photothermal/photodynamic/copper ion synergistic action of a hybrid hydrogel, Biomater. Sci. 6 (8) (2018) 2110–2121.

[29] H. Fan, Y.u. Fan, W. Du, R. Cai, X. Gao, X. Liu, H. Wang, L. Wang, X. Wu, Enhanced type I photoreaction of indocyanine green via electrostatic-force-driven aggregation, Nanoscale. 12 (17) (2020) 9517–9523.

[30] L.-S. Lin, Z.-X. Cong, J.-B. Cao, K.-M. Ke, Q.-L. Peng, J. Gao, H.-H. Yang, G. Liu, X. Chen, Multifunctional Fe3O4@ polydopamine core–shell nanocomposites for intracellular mRNA detection and imaging-guided photothermal therapy, ACS Nano 8 (4) (2014) 3876–3883.

[31] B.-Q. Chen, R.K. Kankala, Y. Zhang, S.-T. Xiang, H.-X. Tang, Q.i. Wang, D.-Y. Yang, S.-B. Wang, Y.S. Zhang, G. Liu, A.-Z. Chen, Gambogic acid augments black phosphorus quantum dots (BPQDs)-based synergistic chemo-photothermal therapy through downregulating heat shock protein expression, Chem. Eng. J. 390 (2020) 124312, https://doi.org/10.1016/j.cej.2020.124312.

[32] Q.i. Xin, H. Shah, A. Nawaz, W. Xie, M.Z. Akram, A. Batool, L. Tian, S.U. Jan, R. Boddula, B. Guo, Q. Liu, J.R. Gong, Antibacterial carbon-based nanomaterials, Adv. Mater. 31 (45) (2019) 1804838, https://doi.org/10.1002/adma.v31.4510.1002/adma.201804838.

[33] B. Geng, D. Yang, D. Pan, L. Wang, F. Zheng, W. Shen, C. Zhang, X. Li, NIR-responsive carbon dots for efficient photothermal cancer therapy at low power densities, Carbon 134 (2018) 153–162.

[34] M. Wu, J. Zhan, B. Geng, P. He, K. Wu, L. Wang, G. Xu, Z. Li, L. Yin, D. Pan, Scalable synthesis of organic-soluble carbon quantum dots: superior optical properties in solvents, solids, and LEDs, Nanoscale. 9 (35) (2017) 13195–13202.

[35] E. Fuente, J. Menéndez, M. Díez, D. Suárez, M. Montes-Morán, Infrared spectroscopy of carbon materials: a quantum chemical study of model compounds, J. Phys. Chem. B 107 (2003) 6350–6359.

[36] S. Suganuma, K. Nakajima, M. Kitano, D. Yamaguchi, H. Kato, S. Hayashi, M. Hara, Hydrolysis of cellulose by amorphous carbon bearing SO3H, COOH, and OH groups, J. Am. Chem. Soc. 130 (38) (2008) 12787–12793.

[37] G. Yang, X. Wan, Y. Su, X. Zeng, J. Tang, Acidophilic S-doped carbon quantum dots derived from cellulose fibers and their fluorescence sensing performance for metal ions in an extremely strong acid environment, J. Mater. Chem. A 4 (33) (2016) 12841–12849.

[38] Y.P. Wu, S. Fang, Y. Jiang, R. Holze, Effects of doped sulfur on electrochemical performance of carbon anode, J. Power Sources 108 (1-2) (2002) 245–249.

[39] A. Munir, T.u. Haq, A. Qurashi, H.u. Rehman, A. Ul-Hamid, I. Hussain, Ultrasmall Ni/NiO nanoclusters on thiol-functionalized and-exfoliated graphene oxide nanosheets for durable oxygen evolution reaction, ACS Applied Energy Materials. 2 (1) (2019) 363–371.

[40] A. Sharma, T. Gadly, S. Neogy, S.K. Ghosh, M. Kumbhakar, Molecular origin and self-assembly of fluorescent carbon nanodots in polar solvents, The journal of physical chemistry letters. 8 (5) (2017) 1044–1052.

[41] M. Sudolská, M. Dubecký, S. Sarkar, C.J. Reckmeier, R. Zbořil, A.L. Rogach, M. Otyepka, Nature of absorption bands in oxygen-functionalized graphitic carbon dots, The Journal of Physical Chemistry C. 119 (23) (2015) 13369–13373.

[42] F. Huo, W. Liang, Y. Tang, W. Zhang, X. Liu, D. Pei, H. Wang, W. Jia, P. Jia, F. Yang, Full-color carbon dots with multiple red-emission tuning: on/off sensors, in vitro and in vivo multicolor bioimaging, J. Mater. Sci. 54 (9) (2019) 6815–6825.

[43] Y. Wang, Q. Su, X. Yang, Exploration of the synthesis of three types of multicolor carbon dot originating from isomers, Chem. Commun. 54 (80) (2018) 11312–11315.

[44] Q. Niu, K. Gao, Z. Lin, W. Wu, Amine-capped carbon dots as a nanosensor for sensitive and selective detection of picric acid in aqueous solution via electrostatic interaction, Anal. Methods 5 (21) (2013) 6228, https://doi.org/10.1039/c3ay41275j.

[45] H. Liu, X. Lv, J. Qian, H. Li, Y. Qian, X. Wang, X. Meng, W. Lin, H. Wang, Graphitic Carbon Nitride Quantum Dots Embedded in Carbon Nanosheets for Near-Infrared Imaging-Guided Combined Photo-Chemotherapy, ACS Nano 14 (10) (2020) 13304–13315.

[46] S. Hu, Q. Zhao, Q. Chang, J. Yang, J. Liu, Enhanced performance of Fe 3+ detection via fluorescence resonance energy transfer between carbon quantum dots and Rhodamine B, RSC Adv. 4 (77) (2014) 41069–41075.

[47] S.A. Raza, S.Q. Naqvi, A. Usman, J.R. Jennings, Y.W. Soon, Spectroscopic study of the interaction between rhodamine B and graphene, J. Photochem. Photobiol., A 418 (2021) 113417, https://doi.org/10.1016/j.jphotochem.2021.113417.

[48] J. Huang, J. Lu, Y. Zhang, S. Xie, G. Lin, W. Lin, P. Zhuang, Z. Zhu, S. Guo, S. Zhang, Q.i. Ge, X. Zhang, W. Cai, Vertically Oriented Graphene for the Fluorescence Quenching Raman Spectra of Aromatic Dyes, The Journal of Physical Chemistry C 125 (27) (2021) 14891–14896.

[49] I. Moreno-Villoslada, M. Jofré, V. Miranda, P. Chandía, R. González, S. Hess, B. L. Rivas, C. Elvira, J. San Román, T. Shibue, H. Nishide, π-Stacking of rhodamine B onto water-soluble polymers containing aromatic groups, Polymer 47 (19) (2006) 6496–6500.

[50] P. Devi, S. Saini, K.-H. Kim, The advanced role of carbon quantum dots in nanomedical applications, Biosens. Bioelectron. 141 (2019) 111158, https://doi.org/10.1016/j.bios.2019.02.059.

[51] C. Zhao, X. Wang, L. Wu, W. Wu, Y. Zheng, L. Lin, S. Weng, X. Lin, Nitrogen-doped carbon quantum dots as an antimicrobial agent against Staphylococcus for the treatment of infected wounds, Colloids Surf., B 179 (2019) 17–27.

[52] D. Lee, C. Lee, W. Kwon, S. Beack, C. Kim, in: N-doped carbon nanodots for non-invasive photoacoustic imaging and photothermal therapy, International Society for Optics and Photonics, 2017, p. 1006433.

[53] J. Ge, Q. Jia, W. Liu, M. Lan, B. Zhou, L. Guo, H. Zhou, H. Zhang, Y. Wang, Y. Gu, X. Meng, P. Wang, Carbon dots with intrinsic theranostic properties for bioimaging, red-light-triggered photodynamic/photothermal simultaneous therapy in vitro and in vivo, Adv. Healthcare Mater. 5 (6) (2016) 665–675.

[54] M. Lan, S. Zhao, Z. Zhang, L.i. Yan, L. Guo, G. Niu, J. Zhang, J. Zhao, H. Zhang, P. Wang, G. Zhu, C.-S. Lee, W. Zhang, Two-photon-excited near-infrared emissive carbon dots as multifunctional agents for fluorescence imaging and photothermal therapy, Nano Res. 10 (9) (2017) 3113–3123.

[55] P. Marbaniang, S. Ingavale, P. Karuppanan, A. Swami, B. Kakade, Rationale approach of nitrogen doping at defect sites of multiwalled carbon nanotubes: a strategy for oxygen reduction electrocatalysis, Int. J. Hydrogen Energy 46 (17) (2021) 10268–10280.

[56] M. Zheng, Y. Li, S. Liu, W. Wang, Z. Xie, X. Jing, One-pot to synthesize multifunctional carbon dots for near infrared fluorescence imaging and photothermal cancer therapy, ACS Appl. Mater. Interfaces 8 (36) (2016) 23533–23541.

[57] Y. Li, X. Zhang, M. Zheng, S. Liu, Z. Xie, Dopamine carbon nanodots as effective photothermal agents for cancer therapy, RSC Adv. 6 (59) (2016) 54087–54091.

[58] S. Zhao, L.i. Yan, M. Cao, L.i. Huang, K.e. Yang, S. Wu, M. Lan, G. Niu, W. Zhang, Near-Infrared Light-Triggered Lysosome-Targetable Carbon Dots for Photothermal Therapy of Cancer, ACS Appl. Mater. Interfaces 13 (45) (2021) 53610–53617.

[59] F.A. Permatasari, H. Fukazawa, T. Ogi, F. Iskandar, K. Okuyama, Design of pyrrolic-N-rich carbon dots with absorption in the first near-infrared window for photothermal therapy, ACS Applied Nano Materials. 1 (5) (2018) 2368–2375.

[60] X. Bao, Y.e. Yuan, J. Chen, B. Zhang, D.i. Li, D. Zhou, P. Jing, G. Xu, Y. Wang, K. Holá, D. Shen, C. Wu, L. Song, C. Liu, R. Zbořil, S. Qu, In vivo theranostics with near-infrared-emitting carbon dots—highly efficient photothermal therapy based on passive targeting after intravenous administration, Light Sci. Appl. 7 (1) (2018), https://doi.org/10.1038/s41377-018-0090-1.

[61] Q. Jia, X. Zheng, J. Ge, W. Liu, H. Ren, S. Chen, Y. Wen, H. Zhang, J. Wu, P. Wang, Synthesis of carbon dots from Hypocrella bambusae for bimodel fluorescence/photoacoustic imaging-guided synergistic photodynamic/photothermal therapy of cancer, J. Colloid Interface Sci. 526 (2018) 302–311.

[62] Y. Li, G. Bai, S. Zeng, J. Hao, Theranostic carbon dots with innovative NIR-II emission for in vivo renal-excreted optical imaging and photothermal therapy, ACS Appl. Mater. Interfaces 11 (5) (2019) 4737–4744.

[63] S. Wen, T. Wu, H. Long, L. Ke, S. Deng, L. Huang, J. Zhang, S. Tan, Mechanism Insight into Rapid Photodriven Sterilization Based on Silver Bismuth Sulfide Quantum Dots, ACS Appl. Mater. Interfaces 13 (18) (2021) 21979–21993.

[64] H. Liu, J. Li, X. Liu, Z. Li, Y.u. Zhang, Y. Liang, Y. Zheng, S. Zhu, Z. Cui, S. Wu, Photo-Sono Interfacial Engineering Exciting the Intrinsic Property of Herbal Nanomedicine for Rapid Broad-Spectrum Bacteria Killing, ACS Nano 15 (11) (2021) 18505–18519.

[65] Y.W. Kwon, J.I. Jin, Characterizations of damages of DNA caused by plasma treatment and reactive species formed thereby, Polym. Adv. Technol. 26 (2015) 762–770.

[66] D. Han, M. Ma, Y. Han, Z. Cui, Y. Liang, X. Liu, Z. Li, S. Zhu, S. Wu, Eco-friendly hybrids of carbon quantum dots modified MoS2 for rapid microbial inactivation by strengthened photocatalysis, ACS Sustainable Chem. Eng. 8 (1) (2020) 534–542.